

Learning-Based Damage Recovery for Healable Soft Electronic Skins

Seppe Terryn,* David Hardman, Thomas George Thuruthel, Ellen Roels, Fatemeh Sahraeeazartamar, and Fumiya Iida

Natural agents display various adaptation strategies to damages, including damage assessment, localization, healing, and recalibration. This work investigates strategies by which a soft electronic skin can similarly preserve its sensitivity after multiple damages, combining material-level healing with software-level adaptation. Being manufactured entirely from self-healing Diels–Alder matrix and composite fibers, the skin is capable of physically recovering from macroscopic damages. However, the simultaneous shifts in sensor fiber signals cannot be modeled using analytical approaches because the materials viscoelasticity and healing processes introduce significant nonlinearities and time-variance into the skin's response. It is shown that machine learning of five-layer networks after 5000 probes leads to highly sensitive models for touch localization with 2.3 mm position and 95% depth accuracy. Through health monitoring via probing, damage and partial recovery are localized. Although healing is often successful, insufficient recontact leads to limited recovery or complete loss of a fiber. In these cases, complete resampling and retraining recovers the networks' full performance, regaining sensitivity, and further increasing the system's robustness. Transfer learning with a single frozen layer provides the ability to rapidly adapt with fewer than 200 probes.

1. Introduction

Soft sensors made of highly deformable materials are one of the enabling technologies in developing a number of soft robotic systems^[1] and wearable devices.^[2–4] They are typically used to measure contact, deformation, pressure, and stress information based on an electrical response to a mechanical stimulus. Sensing mechanisms include conductive liquids,^[5] elastomeric composites with conductive fillers,^[6] ionic hydrogels,^[7] and optical fibers.^[6,8] As these sensors are designed to undergo large deformations over repeated cycles, they are susceptible to fatigue and degradation over time, and are easily damaged by sharp objects. Using self-healing functional materials can therefore improve the reliability, stability, and long-term performance of these soft sensors.^[9–12]

Recently, there has been increasing interest in the development of self-healing materials for soft robotic applications.^[13]

Self-healing polymers can be used for structural support,^[14] as functional soft actuators^[15,16] or as electronic components.^[10,12] Self-healing electronic devices can range in complexity from conducting wires,^[17] to semiconductors and dielectric materials^[18,19] and to sensing elements.^[20–23]


One of the earliest works on a self-healing sensor used a piezoresistive composite made of μNi particles and a self-healing polymeric material.^[21] Similarly, piezoresistive composites with better electrical properties were developed using different functional conductive materials.^[24,25] These sensors change their electrical properties in response to a strain signal and can hence be used for proprioception, force estimation, and contact localization. Hardman et al. used the piezoresistive response of an ionic gelatin/glycerol hydrogel to develop self-healing soft strain sensors for pneumatic actuators.^[26] Contact localization and force sensing can also be done with soft self-healing capacitive sensors.^[27] Capacitive sensing technologies, however, require more involved electronic hardware and suffer from parasitic capacitive effects. Other types of self-healing sensors include temperature sensors,^[28] chemical sensors,^[29] and damage detection sensors.^[30] All demonstrate the recovery of electrical properties after damage, but have not investigated the modeling of these sensors and the functional integrity of these models after a damage–heal cycle.

S. Terryn, E. Roels
Brubotics

Vrije Universiteit Brussel (VUB) and IMEC
Pleinlaan 2, 1050 Brussels, Belgium
E-mail: seterryn@vub.be

S. Terryn, D. Hardman, T. G. Thuruthel, F. Iida
Bio-Inspired Robotics Lab
University of Cambridge
Trumpington Street, Cambridge CB2 1PZ, UK

F. Sahraeeazartamar
Physical Chemistry and Polymer Science (FYSC)
Vrije Universiteit Brussel (VUB)
Pleinlaan 2, 1050 Brussels, Belgium

 The ORCID identification number(s) for the author(s) of this article can be found under <https://doi.org/10.1002/aisy.202200115>.

© 2022 The Authors. Advanced Intelligent Systems published by Wiley-VCH GmbH. This is an open access article under the terms of the Creative Commons Attribution License, which permits use, distribution and reproduction in any medium, provided the original work is properly cited.

DOI: 10.1002/aisy.202200115

Soft robotic sensors present numerous challenges in their modeling. This is because they tend to be responsive to multiple physical cues, exhibit temporal nonlinearities (hysteresis and drift), and their properties are linked to the surrounding matrix.^[2] As extensively demonstrated in this work, these undesired dynamic effects are particularly present in healable soft sensors because they are manufactured out of dynamic reversible polymers and have a viscoelastic behavior. In addition, partial recoveries after healing lead to new sensor behaviors, requiring recalibration. Hence, learning-based approaches, which are becoming increasingly popular in sensor modeling,^[31,32] can be the enabling technology for healable soft sensors. Deep learning techniques have shown promise for modeling these time-variant sensor properties.^[33,34] Long- and short-term memory networks are typically used to capture drift and hysteresis in the sensors. However, these dynamic networks require a continuous stream of sensor data at a fixed sample rate for state estimation, making them challenging for practical applications. Alternatively, static networks can be used with explicit sensor history^[35] or redundant sensor configuration.^[36] In this work, we use deep static networks for drift and hysteresis compensation. In addition, these learning-based approaches are used to model multisensor electronic skins,^[32] multielectrode piezoresistive sensors,^[37] and electrical impedance tomography (EIT) sensors,^[38] having a complex relationship between their resistances/impedances and location of touch. Although machine learning has its sampling and training cost, it allows to make high-performance electronic skins out of extremely inexpensive conductive polymer composite sheets^[39,40] or carbon electrode fibers,^[41] reducing hardware costs.

We present a deep-learning approach for the modeling of a self-healing skin, composed of eight resistive strain sensors, enabling contact localization and depth perception. Although the presented approach is applicable to a wide variety of self-healing materials and sensor morphologies, a general grid-based sensor morphology is selected, composed of a Diels–Alder polymer matrix and conductive Diels–Alder composite fibers. We show how temporal nonlinearities in the sensor response can be compensated using response history and deep neural networks to provide highly accurate state estimation models. Methods for health monitoring, damage detection, and damage localization are presented. As the healed sensors undergo behavioral transformations, we show that transfer learning techniques can be used to recover functionality, enabling the model to be accurately updated with minimal resampling. Our work is the first demonstration of a complete framework for adapting to damages in a soft bodied system, covering damage detection, localization, healing, and recalibration of internal models.

2. Results

2.1. Design of the Healable Artificial Skin

In this work, a completely healable soft electronic skin is created composed of an insulating self-healing $55 \times 55 \times 5 \text{ mm}^3$ square matrix (Figure 1A, yellow), in which eight conductive fibers (Figure 1A, black) are integrated in a grid-based morphology. These fibers function as resistive strain sensors and have a

diameter of 0.5 mm. The healing of both the polymer matrix and composite fibers is relying on Diels–Alder cross-links in the polymer/composite network, discussed in Section 2.2. Four fibers are embedded straight in the x -directions with a distance of 11 mm between them and at a depth of 2.5 mm. The other fibers are embedded perpendicular to these, in the y -direction, also with a distance of 11 mm between them, but at a depth of 3.5 mm. Consequently, perpendicular fibers do not touch in the matrix. Both the matrix and fiber material are flexible, and consequently the skin acts as a soft sensor network that is bendable and stretchable and can potentially be used in soft robotics, including embedding touch sensing in soft grippers (Figure 1A). Additionally, as both materials are self-healing, the entire electronic skin can be healed.

2.2. Artificial Healing on the Material Level

Finding inspiration in biology, scientists have been developing synthetic materials possessing biomimetic healing abilities.^[42] Many are polymer networks relying on reversible (physico) chemical cross-links, like the equilibrium Diels–Alder reaction between a furan and maleimide (blue and red in Figure 1B).^[43] Two different Diels–Alder polymer networks are synthesized: the nonconductive BMI1400-FT3000-r0.5 material used as matrix and the conductive DPBM-FT5000-r0.6-20wt% CB260 composite used for the fibers (details in Materials and Methods). As these polymers contain the reversible Diels–Alder cross-links, they can both heal. When cuts are made, the Diels–Alder bonds locally break, generating reactive maleimide and furan on the fracture surfaces (Figure 1C). However, being reversible, these covalent bonds can be reformed when bringing the fracture surfaces and reactive maleimide and furan groups back together. Upon excellent contact and limited misalignment of the fracture surfaces, healing can occur even at room temperature.^[44] Nevertheless, microscopic gaps caused by misalignment or imperfect contact can be sealed by heating at a higher temperature (90 °C) which increases mobility in the polymer network.

This remarkable healing capacity can be illustrated via tensile testing (Figure 1D), as well as the stretchability of this Diels–Alder polymer and composite, shown by fracture strains surpassing 100%. Samples are cut in half using a scalpel blade, brought back in contact, and healed by heating to 90 °C for 1 h. When fracturing these healed samples in the tensile test and comparing them to a pristine (undamaged) sample, it is clear that the mechanical properties are recovered after this healing process (Figure 1D). For the polymer (yellow), the fracture stress is recovered with a high healing efficiency of 98%, and fracture not initiating at the healed site. Although the mechanical behavior of the composite (black) is recovered for strains below 90%, the fracture stress is not completely recovered and a healing efficiency of 81% is measured (Figure 1D). In addition, the baseline resistance changed from 285 to 460 Ω , recovering the electrical properties with 60% efficiency. This reduction in healing capacity results from the carbon black C260 fillers, which provide conductivity, but reduce the mobility in the polymer network. Nevertheless, a recovery of the mechanical behavior until strains of 90% provides sufficient recovery for many applications,

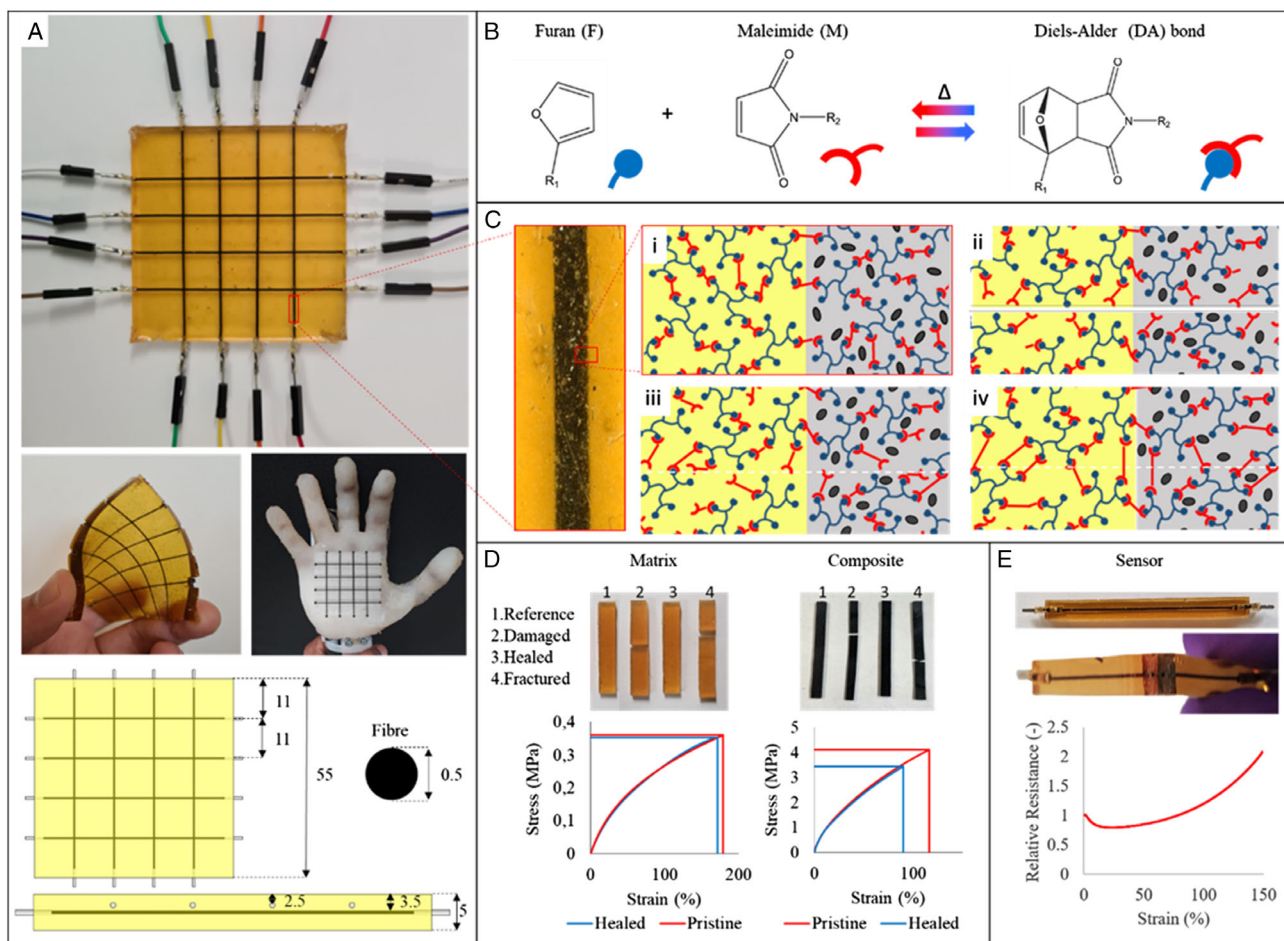


Figure 1. A) The equilibrium reaction between maleimide (red) and furan (blue) forms a reversible Diels–Alder bond. B) The self-healing artificial skin, composed of a sensor network with a grid-based sensor morphology. Eight flexible and healable strain sensors are embedded in the healable matrix. The entire artificial skin is flexible. C) The fiber has a diameter of 0.5 mm and is made from an elastomer that is cross-linked via reversible Diels–Alder bonds and is filled with carbon particles, making it conductive. This fiber is embedded in a Diels–Alder matrix. As both the fibers and the matrix are made from Diels–Alder elastomers, the interface between fiber and matrix is covalently bonded, leading to a high interfacial strength enhancing the sensor performance. D) Both the conductive Diels–Alder composite and nonconductive Diels–Alder matrix are healable due to the presence of reversible Diels–Alder cross-links in their polymer network, as illustrated by recovery of the mechanical properties in a tensile stress strain test with strain ramp of 1% s⁻¹, after being cut completely in half, brought back in contact and healed for 1 h at 90 °C. E) The resistance–strain relationship, obtained from a tensile test on a single strain sensor (55 × 10 × 1 mm³) with a strain ramp of 1% s⁻¹, is nonlinear and is a surjection for the entire strain window. In addition, the loading and unloading curves form a hysteresis loop.

such as healable soft sensors^[10] and embedded heaters for soft robotics or smart wearable devices.^[45]

2.3. Response of the Healable Artificial Skin

Initial tests are performed using a 55 × 10 × 2 mm³ sensor consisting of a conductive DPBM-FT5000-r0.6-20wt%CB260 fiber with a 0.5 mm diameter that is embedded in an insulating BMI1400-FT3000-r0.5 (Figure 1E). Being constructed solely out of self-healing polymers, this entire resistive strain sensor is healable and can even recover from being cut in half, subjecting it to a temperature of 90 °C for 1 h. Upon stretching in a tensile test with fixed strain ramp of 0.01 s⁻¹, the resistance presents a complex surjective relationship with a nonunique mapping

between resistance and strain,^[46] which is challenging to express analytically.

Resistive strain sensors based on conductive elastomeric nanocomposites are not only hard to model due to their high nonlinearity (Figure 1E), but also due to their time-dependent stress/resistive-strain responses caused by the viscoelastic nature of the elastomeric matrix. These effects can be seen in the responses of the skin’s eight sensor fibers when pressed and held at three different locations using a robotic probe (Figure 2A). Conversely, Figure 2B shows the skin’s repeated response when pressed and held at a single location at a depth of 1.5 mm. As the probe moves with a speed of 7 mm s⁻¹ and the probing depth is only 1.5 mm, it is clear that the sensor response is time dependent, indicated by the elastic recovery time of up to 3 s upon release. The relationship between the probing location

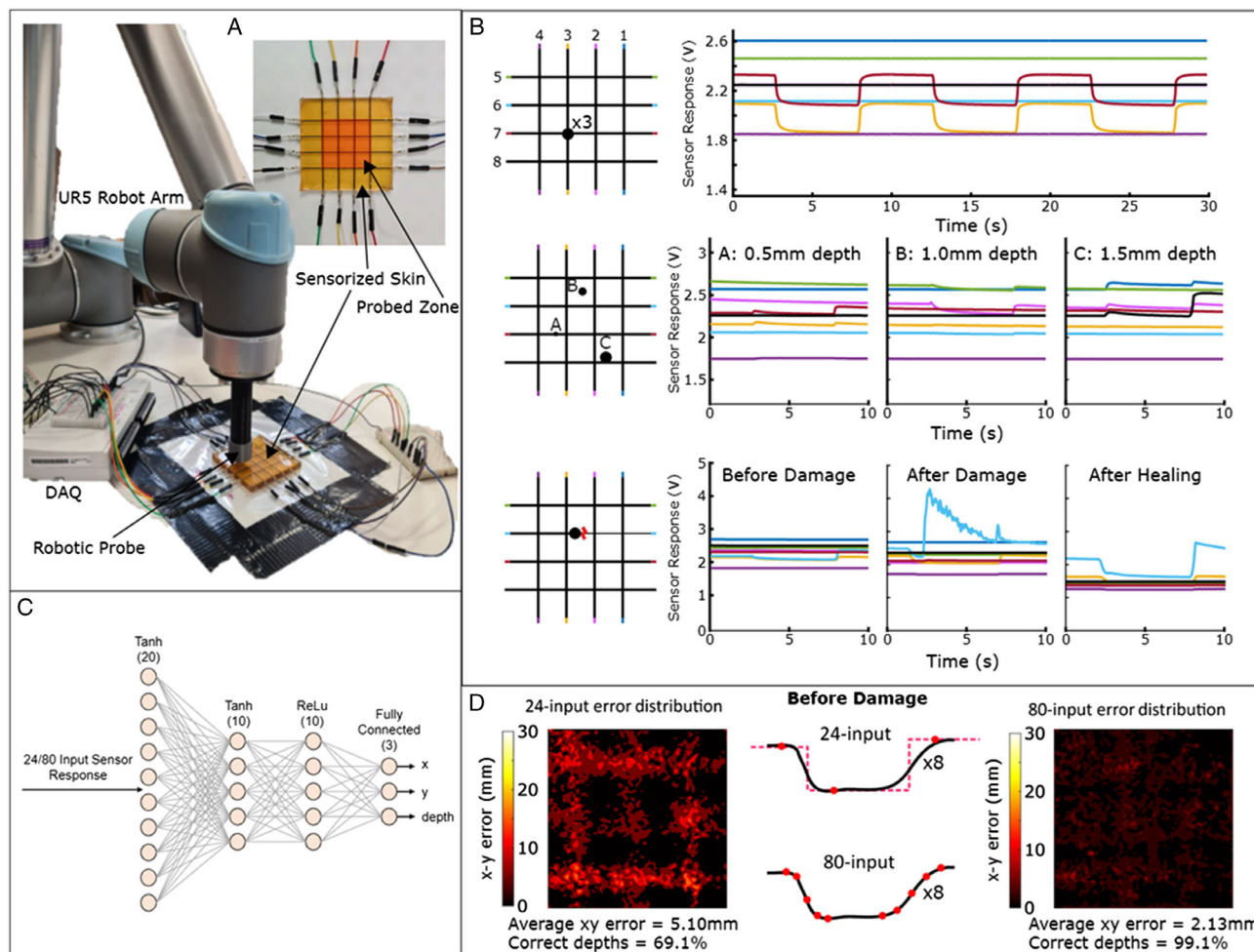


Figure 2. A) The training setup, consisting of a UR5 manipulator from Universal Robots equipped with a cylindrical end effector probe with a diameter of 5 mm. The UR5 probes the soft sensor matrix at different locations within the red zone indicated on the sensor matrix with a depth of 0.5, 1, or 1.5 mm in order to evaluate the skin’s sensitivity. B) The raw signals from the eight sensors while pressing at the location indicated by a black dot on the sensor matrix; i) shows the repeatability of the response to three identical presses. In ii), three locations are probed, each at a different depth. iii) Plots the response to a probe directly next to a damaged area before and after damage and healing. C) The architecture of the deep neural network used throughout this work to map the sensor responses to the predicted x - y location and depth of probing. The size of the input layer can be varied, with the architecture of the output and three hidden layers remain fixed. D) Comparisons of the 24-input and 80-input network performances when trained on 4500 probes of the undamaged skin. The 24-input case first fits a representative square wave to each of the eight sensor’s responses, sampling the three marked locations for the network’s input. The 80-input case uses no signal filtering, and instead directly samples 10 points from each sensor during the press and release of the probe. The x - y error distributions (predicted vs actual) over (A)’s zone are plotted, and the proportion of depths correctly guessed is calculated. The 80-input method is chosen for further use: additional input numbers are tested in Figure S1, Supporting Information.

in the x - y plane (dark orange zone indicated in Figure 2A), the depth, and the sensor response is not easy to model, as already evident by the nonlinear response of the sensor to strain (Figure 1E). This can be seen by the skin’s response to probing at three different locations at varying depths (Figure 2B). Depending on the amount of deformation and its location, the sensor resistance can either increase or decrease, more than two sensors can be activated to a single contact, and the sensors may not return to their initial conditions after probing (due to hysteresis and drift).

Healing of a damage can lead to noncomplete recovery of the mechanical properties (Figure 1D), but also of the sensor

performance. In a third test in Figure 2B, the artificial skin is tested by probing with a depth of 1.5 mm at a single location prior to damage, after damage, and after being healed. Damage is induced using a scalpel blade and slicing completely through one of the sensor fibers. Looking at Figure 2B’s sensor response after damage, it can be seen that the damaged fiber regains electrical contact autonomously after the blade is retracted. This is due to self-sealing, which results from the elastic recovery of the matrix. However, upon probing, the cut reopens leading to a spike to high voltage in the sensor response, indicating that the sensor is still damaged. After healing, the sensor property is regained. However, its response is clearly different from before damage.

It is important to note that the baseline resistances of the undamaged fiber sensors also change after healing. This is probably caused by a slight reconfiguration of the carbon particles/agglomerates in the composite, or by increased contact between the fiber and the crimp connector. Both are induced by a high polymer network mobility, caused by the increase in temperature during the healing process. Due to the influence of healing on the baseline of the sensors, recalibration is necessary in order to preserve the sensitivity of the artificial skin. Altogether, the effects described in this section make the modeling of these healable artificial skin challenging, especially using analytical methods.

2.4. Machine Learning for Contact Localization

The challenges described in previous sections can be circumvented by generating data-driven models of the healable electronic skin. There are two considerations to be made in the design of the learning architecture. First, the network should be able to compensate for the nonlinearities in the sensor response, particularly the ones caused by drift and hysteresis. This is done by appending the inputs to the network with the sensor-response history. Second, the network should be easy and quick to adapt to repeated damage-and-healing cycles. This can be achieved with a sufficiently deep network and transfer learning techniques.^[47]

Figure 2C's network architecture can take either 24 or 80 inputs to predict the location and depth of skin contact, corresponding to either three or ten samples from each of the eight

sensor responses on specific times (see Figure S2, Supporting Information). When three samples are taken, the signal response is first fitted to a square wave, with samples taken before, during, and after contact. Figure 2D shows the *x-y* error magnitude of a network trained on 4500 probes of the undamaged skin, each randomly located and with 0.5, 1.0, or 1.5 mm depth inside the red square (Figure 2A). Uncertainties caused by symmetries in the major sensor responses are visible as a grid of higher errors,^[35] leading to an average error of 5.10 mm for the *x-y* probing position, and the correct depth being identified 69.1% of the time. Contrastingly, the network trained with ten samples from each sensor (Figure 2D) shows a much more uniform and low error of only 2.13 mm while correctly identifying >99% of the probed depths. The training and validation datasets perform extremely similarly (Figure S3, Supporting Information), suggesting that this is not merely a result of overfitting to the test data. The 80-input architecture is selected for further experimentation; as well as lower-error predictions, the samples do not require a square wave to be fitted to the data, and are simply sampled from the raw voltage measurements (Figure 2D).

2.5. Damage Types

In this work, we distinguish three types of damage inside the healable artificial skin. All these damages result from cutting through a single sensor fiber and the surrounding matrix using a scalpel blade (Figure 3A). However, the three differ in the recovery of the system from this damage. 1) In the first case, the sensor fiber regains electrical contact almost immediately

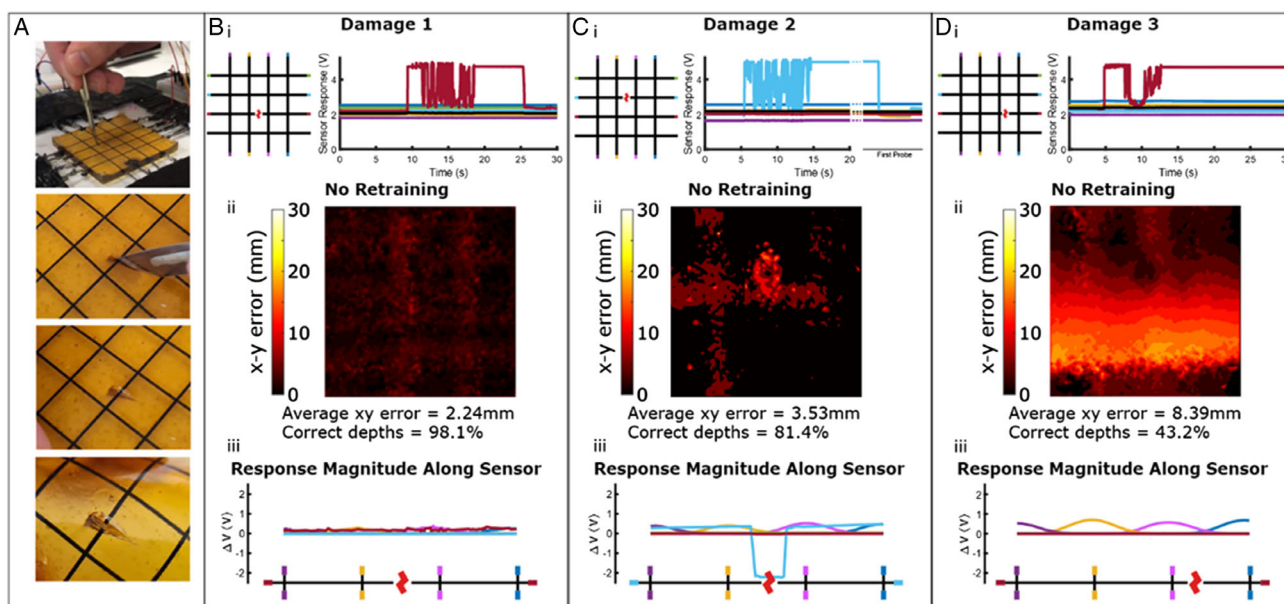


Figure 3. Damage and damage detection in the electronic skin for three damage cases. For each, the damage locations are marked on a representative grid, and the sensor responses to cutting are plotted (see Movie S2, Supporting Information). After damage, 5000 new points are probed (see Figure 2), used to evaluate the performance of a network trained on the skin's behavior before each damage. In addition, in iii, 100 probes are measured along the damaged sensor, and $\Delta V = \left(\frac{V_{\text{before}} + V_{\text{after}}}{2} \right) - V_{\text{during}}$ is calculated at each point for the eight sensors. A) The damages are clean scalpel cuts through the matrix and sensor. B) Damage 1: The sensor is cut, but immediately regains and maintains contact when the scalpel is removed. C) Damage 2: Contact is partially regained shortly after damage—during the first probe—but the sensor still separates and loses the electrical connection when probed close to the damaged area. D) Damage 3: Contact is not regained, and the damaged sensor shows no response.

after retracting the blade (Movie S2, Supporting Information), due to a very clean damage, excellent elastic recovery of the sensor matrix, and negligible misalignment. As a result of excellent contact, the healing takes place instantaneously at room temperature, as described in a previous work.^[44] For this autonomous healing, it is important that contact is regained instantaneously after damage, when the number of reactive maleimide and furan compounds is still high. 2) In the second case, recontact is not achieved immediately, but after some time (Movie S5, Supporting Information) due to slower elastic recovery. During this time, the available reactive maleimide and furan react with one another on separate fracture surfaces. Consequently, healing at the damaged surface is slowed down considerably, e.g., in the order of hours, at room temperature. Nevertheless, this damage can be healed by heating the artificial skin to 90 °C for 1 h. 3) Lastly, in some damage cases, contact is not initially regained. However, upon heating of the artificial skin, an increase in molecular mobility and thermal expansion of the matrix and fibers causes recontact. After recontact, this damage heals during the heating process.

2.6. Health Monitoring, Damage Detection, and Localization

Damages in the artificial skin can be detected by monitoring the resistance of the eight sensors. Upon cutting one of the sensors using a scalpel blade (Figure 3A), its measured resistance becomes infinite and the voltage across the resistor jumps to 5 V. This is done for three damages in two of the eight sensor fibers (Figure 3B–D). By detecting this sharp increase in voltage, the system can easily isolate the damaged sensor line. After the blade is retracted, further tracking of the sensor response allows the detection of recontact due to self-sealing, caused by the elastic recovery of the matrix. This recontact can appear immediately after damage (Figure 3B), in which case the initial sensor state is reached after the blade is retracted. Alternatively, recontact can also be achieved when the skin is touched close to or on the damaged location (Figure 3C). To narrow down the location of damage, the UR5 manipulator probes 100 equally spaced points along the damaged fiber with increments of 0.3 mm while tracking the sensor signal for voltage spikes (Figure 3B). At each location, the difference in voltage during probing and directly before/after probing is calculated and plotted, i.e.

$$\Delta V = \left(\frac{V_{\text{before}} + V_{\text{after}}}{2} \right) - V_{\text{during}} \quad (1)$$

For the first damage, contact is regained immediately and, looking at ΔV along the fiber, it can be seen that the fiber maintains electrical contact, returning a small and relatively constant reading at every location. This measurement suggests that the artificial skin is healed from this damage without the need for a healing procedure that involves heating. For the second damage (Figure 3C), probing along the damaged fiber shows that electrical contact is quickly regained, as the sensor is again sensitive. However, when probing near the damaged region, a loss of electrical contact due to insufficient healing leads to a strong discontinuity in the response. Information from other sensors can also be utilized for localization; clear bumps are visible as the probe passes over sensors aligned with the y -axis. As such, this

probing method allows the identification of the location of damage in the x - y direction. For the third damage (Figure 3D), electrical recontact is not regained after damage, nor during probing. ΔV is zero for the damaged (red) sensor during the entire probing experiments, and the damaged location cannot be further narrowed down.

Damage detection can also be performed by probing the entire x - y plane of the artificial skin. In a second experiment, the UR5 manipulator probes 5000 random x - y coordinates within the red square (Figure 2A), with each randomly allocated to a depth of 0.5, 1.0, or 1.5 mm. After sampling the sensor responses, the probing location and depth are predicted using a network trained prior to damage, in order to highlight the differences in response introduced by the damage. The x - y error is calculated by comparing the estimated probing coordinates to the actual x - y probing position. For the first damage (Figure 3B), only a small increase in error can be detected at the location of damage, illustrating that the sensor is healed without the need for a temperature treatment. For the second damage (Figure 3C), the damage is clearly detected as the area which causes loss of contact when probed, resulting in a region with high error. For the last damage (Figure 3D), the error is large along the entire length of the damaged fiber, as electrical contact is not regained. Although this second damage-detection experiment allows clear visualization of the damage in the x - y plane, probing along the damaged fibers is a much faster method to localize damage. Nevertheless, this extensive probing approach is useful if the damage event is not detected, e.g., when it occurs when the system is offline.

Although it is not always possible to detect the exact location of damage, it is important for the system to investigate in order to facilitate its recovery. In addition, in future applications, including soft robots and smart wearables, tracking of the locations of damage provides important information about parts and locations that are prone to damage. The sensitivity of both touch and damage can be increased by integrating a larger number of sensor fibers into the artificial skin.

2.7. Healing and Retraining

Damages are healed by subjecting the entire artificial skin to a temperature of 90 °C and leaving it for 1 day at 25 °C. From visual inspection in Figure 4A, it can be seen that the damage in matrix and fibers is healed, leaving only a small scar due to misalignment in damages 2 and 3. ΔV along the healed sensors is plotted in Figure 4B–D, to be compared with those of Figure 3. The first damage case shows a reasonably constant response, with a small bump near the damaged area illustrating the residual effect on the sensor's resistance at this location. The constant value is different to that of Figure 3B, reflecting the shift in baseline resistance and responsive properties undergone by all sensors during the temperature treatments. Though the x - y coordinates of each probe can still be localized to within ≈ 3 mm by the network trained on the undamaged sensor, these shifts in resistance cause the proportion of correctly predicted depths to severely drop after healing. This decrease in sensitivity illustrates the importance of health monitoring and damage detection after damage occurs. If the damage is self-sealed and healed at room temperature, the system should not be heated, as this decreases

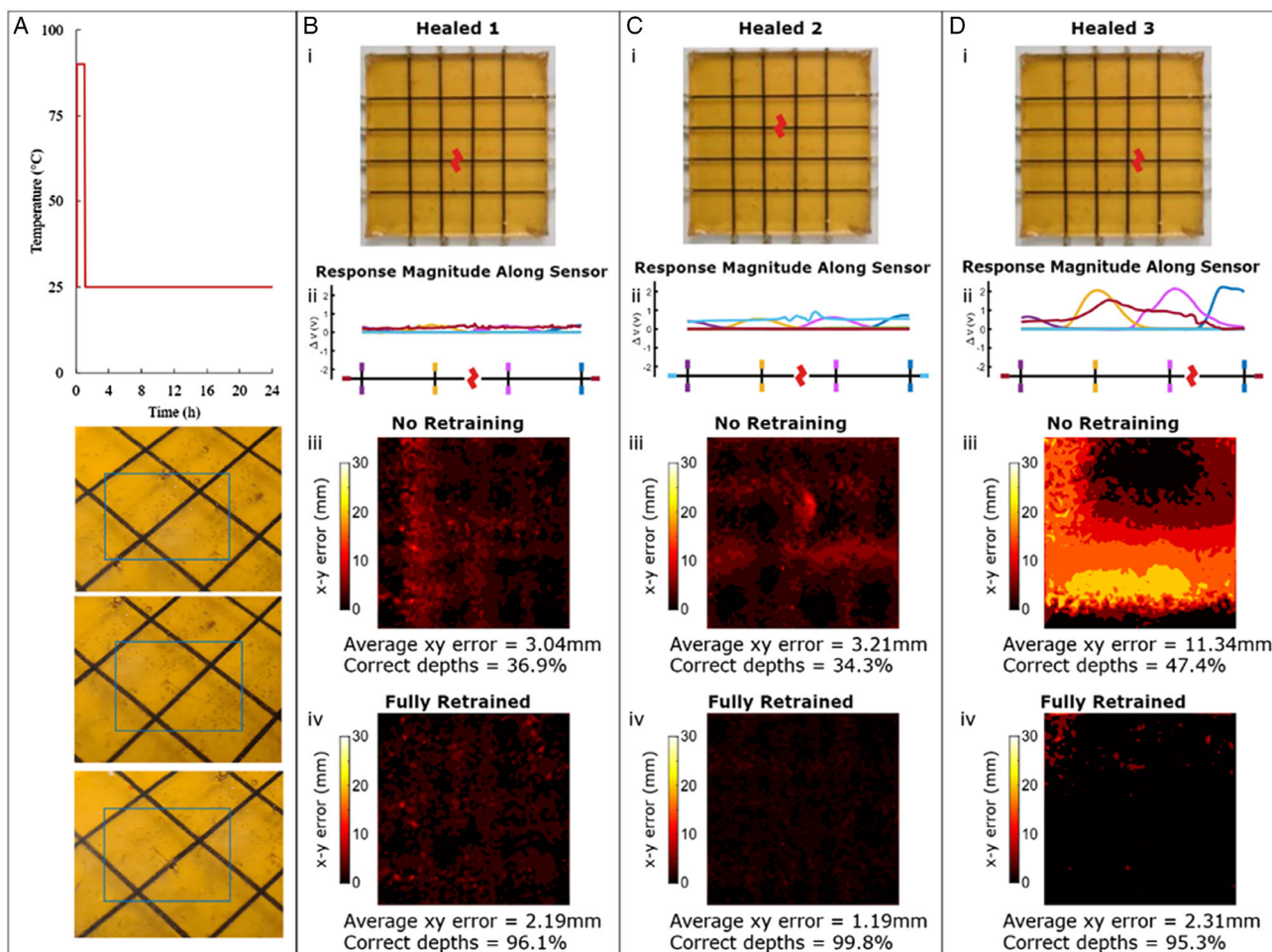


Figure 4. Healing and retraining of the electronic skin. A) The temperature–time profile during healing and images of the healed damages 1, 2, and 3. B–D) Sensitivities of the damaged sensors (B–D in Figure 3) after healing of the three damage cases. In ii, the damaged sensors are probed along their lengths, whereupon the healing of case 2 is particularly clear when compared to the damaged plot. 5000 new points are probed after healing: first the x - y error distributions over the skin are shown for the networks trained before each damage (iii), and then compared (iv) to the errors of new networks trained using these 5000 data points with a 90%:10% training:validation split. In all cases, full retraining results in better x - y localization and depth prediction.

its sensor performance. This decision to continue operation without heating will depend on a thorough health monitoring. Still, given new inputs from the healed skin, the network can adapt to this new behavior—when a new network is fully retrained on the same healed data, 96.1% correct depth predictions are found to be possible (Figure 4B).

In comparison with Figure 3C’s data, Figure 4A’s ΔV plot illustrates the significant improvement in response upon healing of the second damage case. The resistive effects of the damage are still visible (shown in blue), with a small instability in response appearing when the damaged area is probed. However, contact is now maintained throughout probing (Movie S4, Supporting Information), with the response being much more constant along the entire fiber, and showing no significant discontinuity. The healing of this fiber is confirmed by Figure 4C’s sensitivity map before retraining, which shows clear improvement of the sensitivity at the damaged location. Compared to the prehealed map, the average x - y error has

increased, while the correct estimation of the depth has dropped to 34%. This is the result of a change in base resistance after the heat treatment, caused by a slight reconfiguration of the carbon particles/agglomerates in the composite or/and changes in contact resistance at the interface of the fiber and the crimp connector. In order to adapt to this new sensory behavior, the pretrained network must undergo additional training to compensate for these new effects, to prevent the visibly damaged area seen in the error mapping of the “no retraining” evaluation. Full retraining of a network with 4500 new data points from this healed skin is able to attain excellent x - y localization and depth prediction, outperforming even the undamaged network in Figure 2D.

Similarly, the third damage case, which previously showed no sensory response whatsoever, now responds nonlinearly to deformations of the skin (Figure 4D, red curve). However, for the final probing points the sensor response is small, indicating that contact is weak and the fiber is not properly healed. This is emphasized by the sensitivity map before retraining, in which

the damage produces a large average localization error of 11 mm. However, a fully retrained network shows no such error, producing a uniform error distribution which performs comparably to the undamaged skin's network in Figure 2D. This illustrates the redundancy of the electronic skin toward individual sensor damage. This results from a redundancy of sensor fibers and the machine learning-based calibration approach.

This redundancy is further emphasized in Figure S2, Supporting Information, by the performance of a 70-input network trained, validated, and tested on the skin after the first damage case. For each, one of the eight sensors' data is entirely removed. The uniform sensitivity maps, <2 mm localization, and $\approx 100\%$ depth predictions illustrate the redundancy provided by multiple sensor responses, enabling the robustness of the skin to single damages. As stated in this previous work,^[35] it is obvious that this redundancy is limited and losses of multiple fibers will decrease sensitivity rapidly, indicating the importance of striving for correct healing on the material level in electronic skins that are damaged for multiple times in application. Although recalibration through full retraining is very successful, it poses challenges in future applications due to extensive sampling. The following section looks at how a pretrained network's prior knowledge can be utilized to quickly produce similarly performing models when additional recalibration data are costly, i.e., avoiding the need for 5000 new data samples after damage/healing.

2.8. Transfer Learning for Healed Skin Recalibration

In the previous section, we saw how changes in sensor properties introduced by the healing process cause significant degradation in the performances of networks trained on the undamaged skin. Networks trained on 4500 new physical sensor responses measured from the healed skin show no such degradation, demonstrating excellent localization and depth prediction capabilities. These secondary networks are trained "from scratch," with no prior knowledge, and thus they require the same amount of data to reach these levels of performance. As discussed in the introductory sections, such full recalibration of a bioinspired soft sensor is likely to be costly in time, resources, and energy. Instead, it is often beneficial to quickly produce a reasonably performing model with minimal recalibration data, avoiding the "downtime" in which no functioning model is available. To investigate this, we continue the training of the undamaged skin's network, which adapts to the healed sensor nonlinearities. In order to encourage the quick convergence of the network on a satisfactory solution, we analyze the performance of transfer learning techniques on two aspects (discussed fully in Materials and Methods): 1) Layer freezing: the learn rates of up to three of the hidden layers are set to zero before training continues, reducing the total number of weights and biases for optimization. 2) Tactical selection: four methods of selecting the x - y coordinates of new samples are compared: arranged in a uniform grid over the surface of the skin; fully random; weighted in 1D such that y coordinates close to the damaged sensor are more likely to be selected; and weighted in 2D, such that points closest to the damaged location are more likely to be selected.

Figure 5 presents the utility of these techniques in adapting to the healed skin based on the average error and the percentage of correct depths, after the two most severe damage cases: cases 2 and 3, represented in Figure 5 and 6, respectively. Gray dotted lines indicate the performance of a network trained with no prior knowledge. Learning with each parameter set is repeated three times; the ranges of the average localization error and depth predictions are marked, with plotted lines following the mean values.

Figure 5 looks at the adaptation of a pretrained network to the second healed case, having been trained on 4500 data points before damage. Without any form of retraining, we have seen from Figure 4A that an average x - y error of 3.21 mm and depth-prediction accuracy of 34.3% are achieved, marked with a horizontal dashed line in the six plots. After being provided with just 49 new sample points, the networks' localization performances generally remain very close to this line, with one exception: the 2D Gaussian method of selection (represented in pink) performs consistently poorly throughout the tests. To explain why, the first plot includes an image of the localization errors when 4900 samples are used for the transfer learning. As the region directly surrounding the damage has been favored during sample selection, a consistently low error is now found here, as designed. However, this comes at the cost of higher error in the lesser sampled areas—in this case, the left, right, and bottom edges of the sensorized skin. This Gaussian method is therefore a good choice when we wish to design a sensor network with areas of higher and lower sensitivity, and could be extended to include more complex 2D functions. As our model focuses on global optimization of sensitivity, the 2D method is not the best option—additional experiments could consider the effect of standard deviation on its performance.

Using one of the remaining transfer learning methods appears to be a much better choice than full retraining when smaller numbers of sampling are favored: all the methods outperform the network with no prior knowledge below approximately 400 sample points; if only depth prediction is necessary, this figure is closer to 1000. As expected, all performances tend to improve as the number of samples increases, and the benefits of full retraining over a quicker transfer method only become significant when thousands of sample points are available.

There is surprisingly little difference between the performances of the grid, random, and weighted methods—especially at higher sample points. It should be noted that the 1D weighted implementation is less severe than that of the underperforming 2D Gaussian method. The fact that only the 2D method is clearly separate from the others suggests that global, rather than local, calibration is necessary for successful short-term transfer. Provided the network continues learning from a sufficiently uniform distribution over the skin plane, the method of selection (grid, random, or weighted) does not appear to make a significant difference.

Figure 5's three columns consider the magnitude of layer freezing upon performance, setting the learn rates of one, two, or three of the hidden layers to zero before transfer learning commences. In the extremely short term (49/100 sample points), freezing all 3 layers—leaving only the output layer to be adapted—produces the best-performing network. Indeed, the

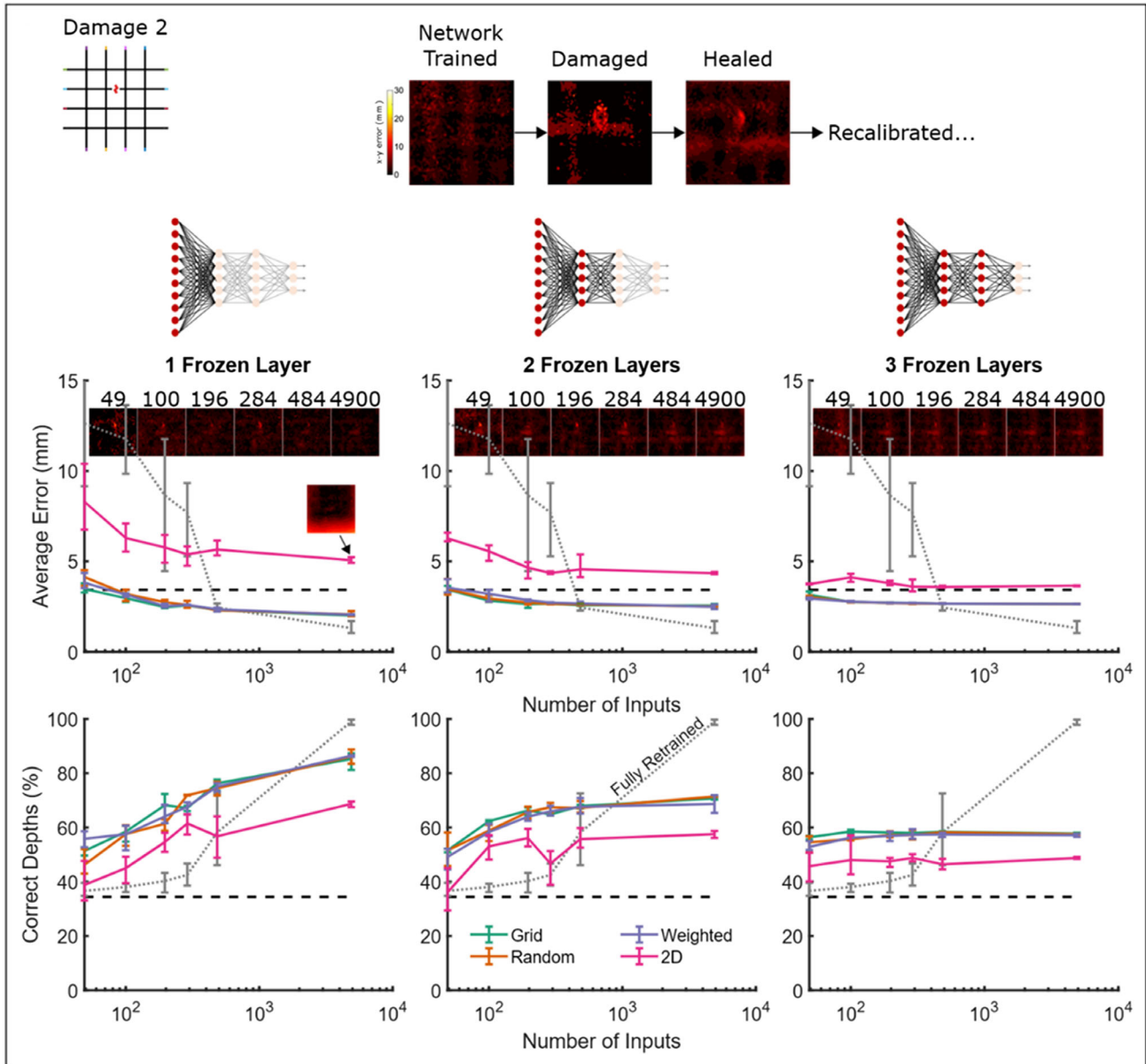


Figure 5. Performance of the networks' transfer learning for damage 2. After “freezing” the weights of selected fully connected layers, training of the networks is continued using 49, 100, 196, 284, 484, or 4900 new data points. Four methods of selecting these points—grid, random, weighted, and 2D (see methods)—are compared to the “fully retrained” performance which has no prior knowledge. A dashed horizontal line represents the performance of the pretrained networks before transfer learning begins (i.e., number of sample points = 0). Example mappings of *x-y* localization error are shown for the random selection method.

49-sample grid, random, and weighted methods of the first two columns show slight decreases in localization performance compared to the zero-sample case, while three frozen layers consistently improve localization. However, the limited change in input→output mapping that can be changed using only the third layer weights leads to a quick saturation of this column's performance, while the single frozen layer continues to improve for larger samples. Unsurprisingly, two frozen layers produce a set of results lying between these two extremes, forming a

reasonable compromise when the number of available sample points is unknown.

Figure 6 shows a similar set of patterns in adapting to the more severe damage/healed case. Again, the 2D method does not satisfactorily converge, overfitting to the damaged area at the expense of sensitivity in more remote regions. The remaining three more uniformly distributed transfer methods are near-indistinguishable, outperforming the fully retrained network for fewer than ≈ 1000 samples. However, 49 samples are now

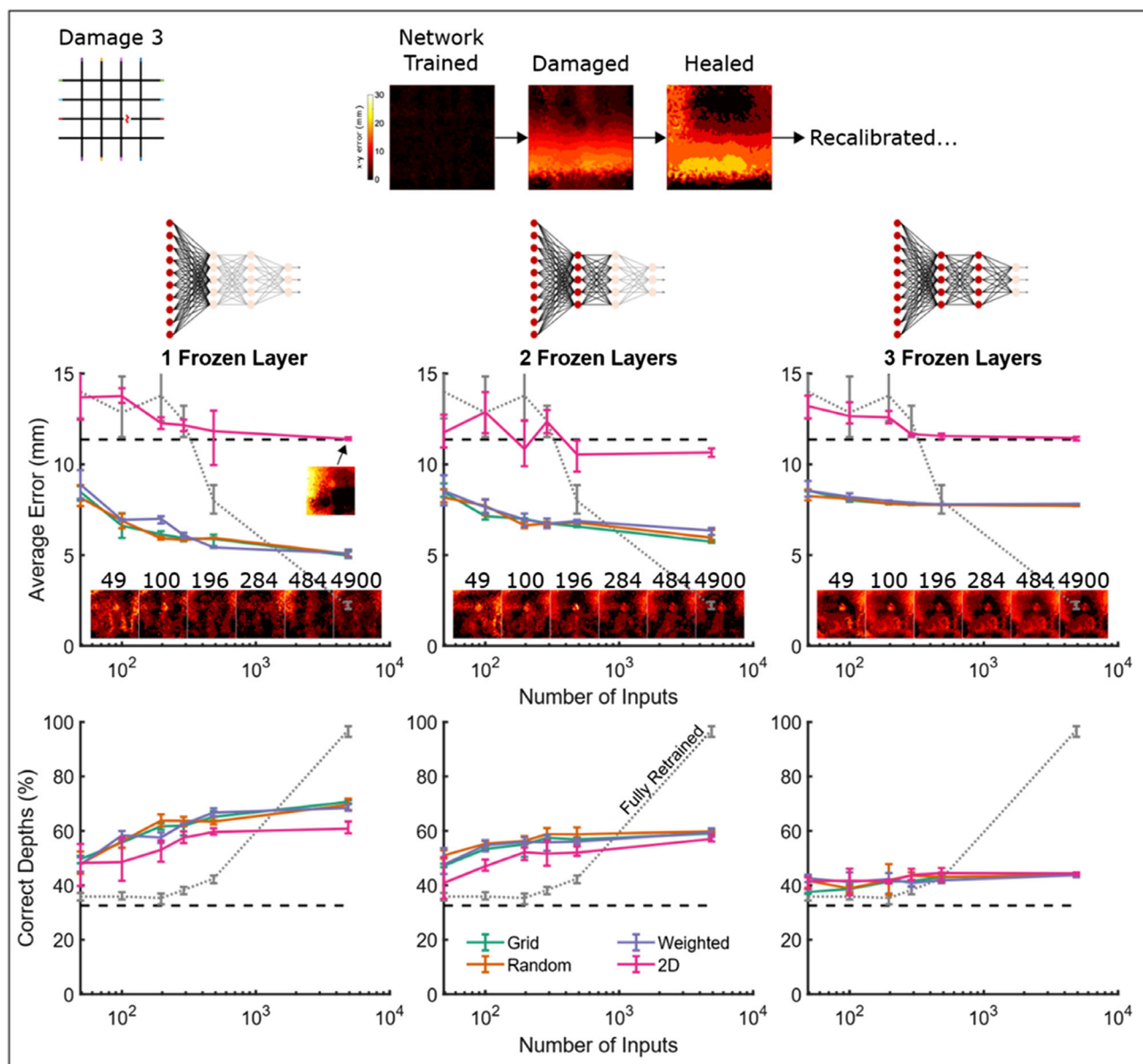


Figure 6. Performance of the networks' transfer learning for damage 3. After “freezing” the weights of selected fully connected layers, training of the networks is continued using 49, 100, 196, 284, 484, or 4900 new data points. Four methods of selecting these points—grid, random, weighted, and 2D (see methods)—are compared to the “fully retrained” performance which has no prior knowledge. A dashed horizontal line represents the performance of the pretrained networks before transfer learning begins (number of sample points = 0). Example mappings of x-y localization error are shown for the random selection method.

sufficient for all three methods to significantly improve upon the zero-sample case; the localization maps show that the region of significant error above the damaged sensor quickly vanishes, and could simply be the result of small shifts in baseline resistance. As such, freezing all three layers is no longer the best approach for small sample sizes, and the 1 frozen layer network produces the best performance in every case. Its greatest improvement upon the fully retrained network occurs with 196 samples, where the random transfer learning technique improves the average localization accuracy by 7.9 mm, and the accuracy of depth predictions by 28.4%.

3. Discussion

Although many studies have proven the potential of healable soft sensors, all these works are limited to the recovery of electrical properties after damage and have not investigated the functional integrity of the sensors after a damage–heal cycle. This is mainly because of the challenges involved in modeling these highly nonlinear and time-variant polymer composites. The proposed learning-based framework circumvents this challenge using real-world experience. The use of deep neural networks with sensor responses resulted in a high-resolution electronic skin

able to localize touch with a high resolution of 2 mm and a correct depth estimation of nearly 100%, even with these highly nonlinear healable sensor fibers. This clearly illustrates the capacity of machine learning, which use will be inevitable in the calibration of many future healable soft sensors.

In order to truly enhance longevity of healable sensors and the systems in which they are embedded, healing of damages should involve minimal sensitivity deterioration. Although full restoration of the sensor response at room temperature is possible upon excellent recontact, its recovery is highly influenced by the slightest misalignment or insufficient contact. In future applications that demand autonomous healing and multiple damage–healing cycles, these nonoptimal recontacts will be unavoidable. In these cases, healing by heating can fill the resulting microscopic cavities, increasing the contact, and the healing efficiency. However, this thermal treatment impacts the base resistance and the sensor response of the healed fiber and the undamaged fibers. Consequently, the sensitivity decreases and in particular the depth estimation becomes unreliable. In these cases, recalibration is inevitable to preserve sensor sensitivity.

In this article, it is shown that full resampling and retraining of the network on the healed electronic skin regains original performance, and even improves it in some cases. In addition, the proposed approach also allows us to exploit redundancies in the system upon loss of a sensor fiber, which provides an additional temporary robustness to damages. This is, however, limited, as the loss of multiple fibers will eventually drive down accuracy, highlighting the need for physical healing abilities, in particular for applications where damage is recurrent. Consequently, the authors believe that the combination of machine learning and self-healing can provide robust and long-lived soft sensorized systems able to cope with multiple types of damage via healing on the material level and adaptation on the software level.

Although training from scratch is reliable, it limits future applications as it will be time-consuming and costly. Though not explored in this work, the authors expect the “press-and-release” method of sampling to be relatively robust to changes in press duration, enabling quicker sampling procedures to be designed. Ultimately, this will be limited by the recovery period of the material. Second, to eliminate unnecessary recalibration, health monitoring is extremely important. As presented in the article, damage can be detected by monitoring the loss of electrical contact of the fiber resistances, while damage localization in the millimeter scale can be performed by probing along the damaged fiber. This can also detect if the damage is healed autonomously at room temperature. For these damages, heating is not required as it would not further increase recovery; on the contrary, it decreases sensitivity and results in the need for recalibration. In addition, in actual future applications, including soft robots and smart wearables, tracking the locations of damage provides important information about parts and locations that are prone to damage.

The introduced transfer learning approach presents a fast alternative for model adaptation with reduced data points. Freezing a higher number of layers in the network is desirable when working with fewer data points and vice versa. The advantages of the proposed transfer learning approach will become more relevant as the sensor network becomes increasingly larger. In such cases, the amount of data required for full training would

be much higher. Additionally, damages and healing would be more localized, implying that a larger chunk of the prior model can be recycled. In that scenario, the resampling algorithm can also become relevant, which is not found in our experiments. Targeting the sampling near to the damage area, or around the damaged sensor, did not lead to improved transfer learning compared to random sampling. This is due to the change in baseline resistance of all fibers due to heating, leading to changes in sensory response throughout the entire skin. Consequently, the resampling and retraining strategy will highly depend on the application in which the sensor skin is used and the time at which damages occur. Transfer learning with a high number of frozen layers can be used to restart operation quickly after healing, with a slightly reduced performance. On the other hand, full retraining can be performed during inactive periods of the system as it requires more time, eventually recovering full sensitivity of the electronic skin.

Although polymeric soft sensors and electronic skins can be produced very cheaply, the authors believe that recovery of the skin after damage through material-based healing whether or not in combination with compensation through recalibration can provide an economic alternative to replacement in various future applications. This is the case when electronic skins are integrated in complex systems. Although the components can be cheap, replacement or maintenance can still be very expensive, due to extensive (dis)assembly. These disassembly issues are exacerbated by the fact that creating modular, scalable soft robots and systems is very challenging, and components are generally irreversibly bond or cured together. In addition, whereas recovery through healing and adaptation can be done autonomously by the system, replacement will in most cases be done through external intervention. For remote applications and field (soft) robotics, external interventions can be very costly as they would rely on transporting the replacement parts to the system or the system to a repair station. Consequently, the authors believe that the presented combination of material-based healing and software-based adaptation/compensation can be an enabling technology for many soft robotics and soft devices, of which their adoption is currently prevented by their lack of resilience to damage.

4. Experimental Section

Materials: The self-healing material, used to insulate the conductive fibers in the sensor matrix, is composed of a Diels–Alder network polymer. The network is formed by cross-linking between bismaleimide (BMI1400 or DPBM) and furan compounds (FT3000 or FT5000). BMI1400 is a low viscosity bismaleimide oligomer with an average molecular weight of 1715 g mol^{-1} and a maleimide functionality of two and supplied by Capling. DPBM is 1,1-(methylenedi-4,1-phenylene) bismaleimide with a purity of 95% is obtained from Sigma-Aldrich. FT3000 and FT5000 are furan-functionalized Jeffamines, obtained through an epoxy amine reaction between furfuryl glycidyl ether (FGE) and Jeffamine JT3000 or JT5000. JT3000 and JT5000 are polyetheramine obtained from Huntsmann from the Jeffamine T-series triamines, with a molecular weight of respectively 3180 and 5712 g mol^{-1} . FGE has a purity of 97% and is supplied by Sage Chemicals. By mixing two reactive compounds, furan-functionalize Jeffamine JT3000 or JT5000 (Figure 1A,B: blue) and bismaleimide DPBM or BMI1400 (red), the Diels–Alder reaction forms thermoreversible covalent cross-links and an elastomeric polymer network (Figure 1B).

The nonconductive BMI1400-FT3000-r0.5, used as insulating matrix in the sensors, is obtained via polymerization of a mixture of BMI1400 and FT3000 with a maleimide-to-furan stoichiometric ratio r of 0.5. The conductive DPBM-FT5000-r0.6-20wt%CB260, used to manufacture the fibers, is synthesized via solvent casting a mixture of DPBM and FT5000 with a maleimide-to-furan stoichiometric ratio r of 0.6 and 20 wt% carbon black CB260, dissolved in chloroform with a 20 wt%. The synthesis of both of these polymer networks described in detail in Supporting Information 1, Supporting Information.

Healable Artificial Skin: The sensor network (Figure 1D) is a $55 \times 55 \times 5 \text{ mm}^3$ square composed out of BMI1400-FT3000-r0.5 in which eight conductive DPBM-FT5000-r0.6-20wt%CB260 fibers are integrated in a grid-based morphology. Four fibers are embedded straight in the x -directions with a distance of 11 mm between them and at a depth of 2.5 mm. The other fibers are embedded perpendicular to these, in the y -direction, also with a distance of 11 mm between them, but at a depth of 3.5 mm. Consequently, perpendicular fibers do not touch in the matrix. The fibers have a diameter of 0.5 mm and are extruded in a dedicated piston extruder (Supporting Information 2, Supporting Information). The sensor network is manufactured by straightening the fibers in a laser cut PMMA mold, in which a mixture of BMI1400 and FT3000 is poured (Supporting Information 3, Supporting Information). Upon polymerization of this BMI1400-FT3000-r0.5 mixture, the matrix solidifies and the fibers are embedded. During this polymerization, strong covalent Diels–Alder bonds are formed between the fibers and the matrix. At the end of the sensor network, the fibers are connected to jump wires via aluminum crimp connectors.

Characterization: The two Diels–Alder polymer networks are characterized via tensile testing until fracture with a strain ramp of $1\% \text{ s}^{-1}$ on a Dynamic Mechanic Analyzer (DMA) Q800 of TA instruments and sample sizes of $5 \times 30 \times 1 \text{ mm}^3$ for the BMI1400-FT3000-r0.5 samples and $3 \times 30 \times 1 \text{ mm}^3$ for the DPBM-FT5000-r0.6-20wt%CB260. The single resistive strain sensor is characterized on a dedicated tensile testing setup. The sensor network is characterized via training data collected using a UR5 arm from Universal Robots equipped with a cylindrical polylactic acid (PLA) probe end effector with a diameter of 5 mm (Figure 1A). The skin is adhered to a 3 mm PMMA plate, which is secured to the table below the probe. The 3D origin is set above the intersection of sensors 4 and 8 in Figure 2, such that sensor 4 lies in the $x = 0$ plane and sensor 8 lies in the $y = 0$ plane. The $z = 0$ plane is defined at the skin's free surface. All descents and ascents begin from the $z = 10 \text{ mm}$ plane, in which the probe moves between x - y coordinates.

A full characterization of the skin (undertaken after every damage/healing) consists of three parts: 1) Line: (25 min) 100 equally spaced points along the most recently damaged sensor are consecutively probed at a 1.5 mm depth, and all sensor responses are recorded. During each, the probe descends vertically downward at 3.8 mm s^{-1} , is held in place for 5 s, before vertically ascending at 7.7 mm s^{-1} . The setup pauses for 6 s between each probe to minimize the transient effects of the skin's recovery. The 80 inputs to the neural network can be collected at the start of this wait period, and do not depend on its length. The response recoveries are generally observed to take $\approx 1 \text{ s}$, and it is expected that this wait could be significantly shortened in future experiments. Animations of the sensor responses can be found in Movies S3 and S4, Supporting Information. 2) Repeated: (16 min) The closest intersection of 2 points to the damaged location is probed 100 times at a 1 mm depth, and all sensor responses are recorded. The probe descends and ascends at 7.3 mm s^{-1} , pressing for 5 s and leaving 2 s between each press. Animations of the sensor responses can be found in Movies S5 and S6, Supporting Information. 3) Random: (17 h) 5000 random x - y coordinates are generated within the red square of Figure 2A, with each randomly allocated to a depth of 0.5, 1.0, or 1.5 mm. All locations are probed, using the same timings described above (plus additional movement between locations), and all eight sensor responses are recorded. These 5000 responses are used to train the neural networks (90%:10% training:validation split), to plot the error maps, and to calculate the network's performance.

Each of the eight sensors is connected to the ground side of a potential divider, with 120 k Ω resistors completing the connection to a 5 V direct

current (DC) output of a National Instruments multichannel data acquisition module-USB-6212. Throughout the characterization, sensor responses are recorded at the central nodes of the potential dividers, using the USB-6212's analog inputs at a 20 Hz sampling rate. As such, the mapping between a sensor's plotted voltage V and the measured resistance R is described

$$R = 120 \cdot \frac{V}{5 - V} \text{ k}\Omega \quad (2)$$

The 80 inputs of the neural network are sampled from the 8 sensors' raw voltage measurements at ten specific times after the probe begins to descend: 1.25, 1.50, 1.75, 2.00, 2.25, 6.50, 6.75, 7.00, 7.25, and 7.50 s. The 24-input case in Figure 2D instead samples the eight sensor voltages at 1, 3, and 8 s, after using total variation denoising ($\lambda = 15$) to convert the response to a square wave.^[35,48] Intermediate numbers of inputs are considered in Figure S2, Supporting Information: network performances are found to have saturated before the 80-input case, such that higher input numbers are not investigated in this work. Damaging events, e.g., cuts in the sensor network, are recorded using a digital camera.

Healing: Upon excellent contact and limited misalignment of the fracture surfaces, healing can be performed at room temperature.^[44] However, the rebonding and the resulting healing is accelerated by increasing the temperature, which increases both reactivity and kinetics in the dynamic polymer network.^[49] For healing on the material level, on the single sensor level and on the artificial skin level, always the same temperature profile was used; 1 h at 90 °C. Upon cooling to 25 °C and remaining for 24 h, the Diels–Alder bonds rebond, eventually recovering mechanical performance. Heat was provided by placing the damaged parts in a preheated oven at 90 °C.

Deep Neural Network: The same network architecture is used throughout the work, implemented using MATLAB's Deep Learning Toolbox, and is shown in Figure 2C. The preliminary input layer is of size 80 in all cases other than the creation of Figure 2D's 24-input map. Between this and the 3-node regression output (x , y , and depth), three fully connected layers (of sizes 20, 10, 10) are implemented, using tanh, tanh, and ReLU activation functions, respectively.

To train the network on 5000 measured probes, the input dataset is first normalized using the mean and standard deviations of each of the 80 inputs. The corresponding targets are linearly scaled to range between 0 and 1, such that depth and positional accuracies are assigned equal importance. An adaptive moment estimation optimizer is used with 90%:10% training:validation split, 0.05 learn rate, and gradient threshold of 1. Training is terminated when the validation loss (calculated every 30 iterations) does not improve over ten consecutive evaluations. If training exceeds 1250 iterations, the learn rate is dropped to 0.01; training is terminated if 2000 iterations pass. In practice, the only network which does not fulfill the validation criterion before the learn rate drops is that of Figure 4C, as shown in Figure S4, Supporting Information.

Transfer learning is performed by “freezing” a specified number (1, 2, or 3) of the pretrained network's fully connected hidden layers, i.e., setting their learn rates to zero. Training is continued using the parameters described above, with an increased gradient threshold of 10. Four methods are introduced to select a subset of the available data for training and validation, representing the strategic choice of recalibration points after sensor damage and healing: 1) Grid: The x - y coordinates of the selected recalibration points form a geometric grid, with edges corresponding to those of Figure 2A's red zone; only square numbers are tested in Figure 5 and 6, in order to facilitate this. 2) Random: The points are sampled randomly from the available dataset. 3) Weighted: The x coordinate is sampled randomly, whilst the y coordinate is sampled from a truncated Gaussian distribution centered on the damaged sensor, with 15 mm standard deviation. 4) 2D: The coordinates are sampled from a truncated 2D Gaussian, centered at the damaged location with $\sigma = 20 \cdot I_2$.

Once a list of coordinates has been generated for the grid, weighted, and 2D cases, the closest preprobed point is identified, and used as an input for transfer learning. Probing depths remain randomly distributed between 0.5, 1.0, and 1.5 mm.

Supporting Information

Supporting Information is available from the Wiley Online Library or from the author.

Acknowledgements

S.T. and D.H. contributed equally to this work. This work was performed in relation to and funded by the EU FET Open RIA Project SHERO (grant no. 828818). In addition, the authors gratefully acknowledge the FWO (Fonds Wetenschappelijk Onderzoek) for the personal grants of Terryn (grant no. 1100416N) and Roels (grant no. 1S84120N), and EPSRC DTP EP/R513180/1.

Conflict of Interest

The authors declare no conflict of interest.

Author Contributions

S.T., D.H., T.G.T., and F.I.: conceived the conceptual idea of combining self-healing with machine learning to develop electronic skins that preserve their sensitivity after damages, combining material-level healing with software-level adaptation; S.T., D.H., and T.G.T.: designed the methodology and experiments; S.T.: fabricated the electronic skin; S.T., E.R., and F.S.: manufactured the fibers; S.T., D.H., and T.G.T.: did experiments and did data treatment and interpretation; S.T. and D.H.: did the visualization through videos, pictures, and figures for manuscript and Supporting Information; S.T., D.H., and T.G.T.: wrote the original draft of the manuscript. All authors contributed in review and editing. F.I.: did supervision; S.T. and F.I.: did funding acquisition.

Data Availability Statement

The data that support the findings of this study are available in the supplementary material of this article.

Keywords

damage recovery, electronic skins, flexible electronics, machine learning, self-healing, soft sensors, transfer learning

Received: May 6, 2022

Revised: June 28, 2022

Published online: October 31, 2022

- [1] N. Lu, D. H. Kim, *Soft Rob.* **2014**, *1*, 53.
 [2] M. Amjadi, K. U. Kyung, I. Park, M. Sitti, *Adv. Funct. Mater.* **2016**, *26*, 1678.
 [3] H. Wang, M. Totaro, L. Beccai, *Adv. Sci.* **2018**, *5*, 1800541.
 [4] S. Li, X. Zhou, Y. Dong, J. Li, *Macromol. Rapid Commun.* **2020**, *41*, 2000444.
 [5] Y. Park, B. Chen, R. J. Wood, **2012**, *12*.
 [6] M. Amjadi, A. Pichitpajongkit, S. Lee, S. Ryu, I. Park, *ACS Nano* **2014**, *8*, 5154.
 [7] Z. Zhu, H. S. Park, M. C. McAlpine, *Sci. Adv.* **2020**, *6*, 1.
 [8] H. Zhao, J. Jalving, R. Huang, R. Knepper, A. Ruina, R. Shepherd, *IEEE Rob. Autom. Mag.* **2016**, *23*, 55.
 [9] M. Khatib, O. Zohar, H. Haick, *Adv. Mater.* **2021**, *33*, 1.
 [10] J. Kang, J. B. H. Tok, Z. Bao, *Nat. Electron.* **2019**, *2*, 144.

- [11] M. U. Ocheje, B. P. Charron, A. Nyayachavadi, S. Rondeau-Gagné, *Flexible Printed Electron.* **2017**, *2*, 043002.
 [12] Y. J. Tan, J. Wu, H. Li, B. C. K. Tee, *ACS Appl. Mater. Interfaces* **2018**, *10*, 15331.
 [13] S. Terryn, J. Langenbach, E. Roels, J. Brancart, C. Bakkali-Hassani, Q.-A. Poutrel, A. Georgopoulou, T. G. Thuruthel, A. Safaei, P. Ferrentino, *Mater. Today* **2021**, *47*, 187.
 [14] S. Terryn, J. Brancart, D. Lefeber, G. Van Assche, B. Vanderborght, *IEEE Rob. Autom. Lett.* **2017**, *3*, 16.
 [15] P. Zhang, G. Li, *Polymer* **2015**, *64*, 29.
 [16] Z. Feng, J. Hu, H. Zuo, N. Ning, L. Zhang, B. Yu, M. Tian, *ACS Appl. Mater. Interfaces* **2019**, *11*, 1469.
 [17] E. Palleau, S. Reece, S. C. Desai, M. E. Smith, M. D. Dickey, *Adv. Mater.* **2013**, *25*, 1589.
 [18] Y. L. Rao, A. Chortos, R. Pfattner, F. Lissel, Y. C. Chiu, V. Feig, J. Xu, T. Kurosawa, X. Gu, C. Wang, M. He, J. W. Chung, Z. Bao, *J. Am. Chem. Soc.* **2016**, *138*, 6020.
 [19] J. Y. Oh, S. Rondeau-Gagné, Y. C. Chiu, A. Chortos, F. Lissel, G. J. N. Wang, B. C. Schroeder, T. Kurosawa, J. Lopez, T. Katsumata, J. Xu, C. Zhu, X. Gu, W. G. Bae, Y. Kim, L. Jin, J. W. Chung, J. B. H. Tok, Z. Bao, *Nature* **2016**, *539*, 411.
 [20] J. Kang, D. Son, G. J. N. Wang, Y. Liu, J. Lopez, Y. Kim, J. Y. Oh, T. Katsumata, J. Mun, Y. Lee, L. Jin, J. B. H. Tok, Z. Bao, *Adv. Mater.* **2018**, *30*, 1.
 [21] B. C. Tee, C. Wang, R. Allen, Z. Bao, *Nat. Nanotechnol.* **2012**, *7*, 825.
 [22] D. Son, J. Kang, O. Vardoulis, Y. Kim, N. Matsuhisa, J. Y. Oh, J. W. To, J. Mun, T. Katsumata, Y. Liu, A. F. McGuire, M. Krason, F. Molina-Lopez, J. Ham, U. Kraft, Y. Lee, Y. Yun, J. B. H. Tok, Z. Bao, *Nat. Nanotechnol.* **2018**, *13*, 1057.
 [23] Y. Cao, Y. J. Tan, S. Li, W. W. Lee, H. Guo, Y. Cai, C. Wang, B. C. K. Tee, *Nat. Electron.* **2019**, *2*, 75.
 [24] E. D'Elia, S. Barg, N. Ni, V. G. Rocha, E. Saiz, *Adv. Mater.* **2015**, *27*, 4788.
 [25] Y. Yang, B. Zhu, D. Yin, J. Wei, Z. Wang, R. Xiong, J. Shi, Z. Liu, Q. Lei, *Nano Energy* **2015**, *17*, 1.
 [26] D. Hardman, T. George Thuruthel, F. Iida, *NPG Asia Mater.* **2022**, *14*, 1.
 [27] J. Li, J. Liang, L. Li, F. Ren, W. Hu, J. Li, S. Qi, Q. Pei, *ACS Nano* **2014**, *8*, 12874.
 [28] Y. He, S. Liao, H. Jia, Y. Cao, Z. Wang, Y. Wang, *Adv. Mater.* **2015**, *27*, 4622.
 [29] S. Bai, C. Sun, H. Yan, X. Sun, H. Zhang, L. Luo, X. Lei, P. Wan, X. Chen, *Small* **2015**, *11*, 5807.
 [30] T. G. Thuruthel, A. W. Bosman, J. Hughes, F. Iida, *MDPI Sens.* **2021**, *21*, 8284.
 [31] D. Kim, S. H. Kim, T. Kim, B. B. Kang, M. Lee, W. Park, S. Ku, D. W. Kim, J. Kwon, H. Lee, J. Bae, Y. L. Park, K. J. Cho, S. Jo, *PLoS One* **2021**, *16*, 1.
 [32] B. Shih, D. Shah, J. Li, T. G. Thuruthel, Y. L. Park, F. Iida, Z. Bao, R. Kramer-Bottiglio, M. T. Tolley, *Sci. Rob.* **2020**, *5*, eaaz9239.
 [33] S. Han, T. Kim, D. Kim, Y. L. Park, S. Jo, *IEEE Rob. Autom. Lett.* **2018**, *3*, 873.
 [34] T. G. Thuruthel, B. Shih, C. Laschi, M. T. Tolley, *Sci. Rob.* **2019**, *4*, eaav1488.
 [35] T. G. Thuruthel, J. Hughes, F. Iida, *IEEE Sens. J.* **2020**, *20*, 10801.
 [36] T. G. Thuruthel, J. Hughes, A. Georgopoulou, F. Clemens, F. Iida, *IEEE Rob. Autom. Lett.* **2021**, *6*, 2099.
 [37] D. Kong, G. Yang, G. Pang, Z. Ye, H. Lv, Z. Yu, F. Wang, X. V. Wang, K. Xu, H. Yang, **2022**, 2200050.
 [38] Z. Husain, N. A. Madjid, P. Liatsis, *IEEE Sens. J.* **2021**, *21*, 11628.
 [39] K. S. Sohn, J. Chung, M. Y. Cho, S. Timilsina, W. B. Park, M. Pyo, N. Shin, K. Sohn, J. S. Kim, *Sci. Rep.* **2017**, *7*, 1.
 [40] J. W. Lee, J. Chung, M. Y. Cho, S. Timilsina, K. Sohn, J. S. Kim, K. S. Sohn, *ACS Appl. Mater. Interfaces* **2018**, *10*, 20862.

- [41] M. Y. Cho, J. H. Lee, S. H. Kim, J. S. Kim, S. Timilsina, *ACS Appl. Mater. Interfaces* **2019**, *11*, 11910.
- [42] S. Wang, M. W. Urban, *Nat. Rev. Mater.* **2020**, *5*, 562.
- [43] A. Cuvelier, R. Verhelle, J. Brancart, B. Vanderborght, G. Van Assche, H. Rahier, *Polym. Chem.* **2019**, *10*, 473.
- [44] S. Terryn, J. Brancart, E. Roels, G. Van Assche, B. Vanderborght, *IEEE Rob. Autom. Mag.* **2020**, *27*, 44.
- [45] N. Tiwari, Ankit, M. Rajput, M. R. Kulkarni, R. A. John, N. Mathews, *Nanoscale* **2017**, *9*, 14990.
- [46] L. Flandin, A. Hiltner, E. Baer, *Polymer* **2001**, *42*, 827.
- [47] S. J. Pan, Q. Yang, *IEEE Trans. Knowl. Data Eng.* **2010**, *22*, 1345.
- [48] M. A. Little, N. S. Jones, *Proc. R. Soc. A Math. Phys. Eng. Sci.* **2011**, *467*, 3088.
- [49] S. Terryn, J. Brancart, D. Lefeber, G. Van Assche, B. Vanderborght, *Sci. Rob.* **2017**, *2*, eaan4268.